Measuring seismic attenuation in polar firn: method and application to Korff Ice Rise, West Antarctica

Ronan S. Agnew[1,2] (ID), Roger A. Clark[1], Adam D. Booth[1], Alex M. Brisbourne[2] (ID) and Andrew M. Smith[2] (ID)

[1]School of Earth and Environment, University of Leeds, Leeds, UK and [2]NERC British Antarctic Survey, Cambridge, UK

Abstract

We present seismic measurements of the firn column at Korff Ice Rise, West Antarctica, including measurements of compressional-wave velocity and attenuation. We describe a modified spectral-ratio method of measuring the seismic quality factor (Q) based on analysis of diving waves, which, combined with a stochastic method of error propagation, enables us to characterise the attenuative structure of firn in greater detail than has previously been possible. Q increases from 56 ± 23 in the uppermost 12 m to 570 ± 450 between 55 and 77 m depth. We corroborate our method with consistent measurements obtained via primary reflection, multiple, source ghost, and critically refracted waves. Using the primary reflection and its ghost, we find $Q = 53 \pm 20$ in the uppermost 20 m of firn. From the critical refraction, we find $Q = 640 \pm 400$ at 90 m depth. Our method aids the understanding of the seismic structure of firn and benefits characterisation of deeper glaciological targets, providing an alternative means of correcting seismic reflection amplitudes in cases where conventional methods of Q correction may be impossible.

1. Introduction

Investigating the structure of polar firn is important for understanding the response of glaciers and ice sheets to a warming climate. Modelling firn density is necessary for calculating ice sheet mass balance from altimetry measurements (Wingham, 2000; Alley and others, 2007). The mechanical properties of firn are key to understanding processes of crevasse formation (Rist and others, 1996), and potentially have implications for ice shelf rifting and hydrofracture (Kuipers Munneke and others, 2014; Hubbard and others, 2016; Kulessa and others, 2019).

Studying the structure of firn using seismic techniques requires wavelet velocities and amplitudes to be considered. Methods of measuring seismic velocity are well-developed: seismic velocity can be used as a proxy for density (Kohnen, 1972) and can be used to estimate the thickness of the firn column (e.g. Hollmann and others, 2021). Combined estimates of compressional (P) and shear (S) wave velocities can also be used to evaluate mechanical properties such as Poisson's ratio (King and Jarvis, 2007) and elastic moduli (Schlegel and others, 2019). In contrast, tools for quantifying attenuation, derived from amplitude losses, are less well developed. Attenuation is caused by both intrinsic mechanisms (elastic wave energy conversion) and apparent mechanisms (e.g. tuning and scattering); their combined effect is measured using the dimensionless seismic quality factor, or Q (O'Doherty and Anstey, 1971; Schoenberger and Levin, 1974).

Measuring Q is desirable for two main reasons. The first is that correcting for attenuation through firn is an essential part of many glaciological measurements of seismic amplitude. These include amplitude-versus-offset measurements, which are important for identifying glacial substrates (e.g. Peters and others, 2007, 2008; Booth and others, 2012, 2016; Horgan and others, 2021), as well as normal-incidence methods (e.g. Smith, 1997; Muto and others, 2019). However, current methods of measuring attenuation do not take into account the complex attenuative structure of firn, and often rely on the presence of multiple reflections, which are not always present with a sufficient signal-to-noise ratio (e.g. Dow and others, 2013; Muto and others, 2019).

Second, because Q is influenced by the physical properties of the propagating medium, measuring it has the potential to give further insight into the physical structure of firn. For example, the relationship between the compressional- and shear-wave quality factors and velocities in sands has been observed to be influenced by fluid saturation (Prasad and Meissner, 1992), so measuring Q in firn may have implications for characterising firn hydrology. Recent observations of complex firn structure (Hollmann and others, 2021) and large ice lenses within the firn column (Hubbard and others, 2016) highlight the need for continued in-situ characterisation of firn and improvement of existing methods.

Although the continuous increase in seismic velocity with depth enables the velocity-depth structure to be measured in detail by relatively simple methods such as Wiechert–Herglotz inversion (Herglotz, 1907; Wiechert, 1910; Slichter, 1932), constraining the attenuation structure is less straightforward, due to the lack of convenient collinear raypaths. In this paper, we present a novel process of measuring the depth dependence of Q in the firn from diving waves

(downgoing direct waves continuously refracted back towards the surface). We apply the process to data from Korff Ice Rise, West Antarctica, providing a more complete description of the firn's attenuative structure than has previously been possible. We complement these results with measurements made using primary and multiple reflections, their source ghosts, and direct waves, to validate the firn Q model and obtain a complete Q vs depth model for the entire glacier.

1.1. The seismic quality factor of snow, firn and ice

As a seismic wave propagates, it loses energy in three generic ways: geometric spreading, partial reflection at interfaces, and by conversion of kinetic energy to heat due to the internal friction of the propagating medium. The lattermost is termed seismic attenuation, and is quantified using a dimensionless quality factor Q. Q is proportional to the fractional energy loss per wave cycle (Aki and Richards, 2002; Sheriff and Geldart, 1995), with higher Q materials associated with more efficient propagation. A wide range of P-wave quality factors (Q_p) have been measured in both polar ice sheets and mountain glaciers; field-based measurements have ranged from $Q_p = 6 \pm 1$ in warm ice (Gusmeroli and others, 2010), to $Q_p > 500$ in cold polar ice (Bentley and Kohnen, 1976). A dependence of Q_p on temperature has been demonstrated both in the laboratory (Kuroiwa, 1964), and in the field (Peters and others, 2012, using a method by Dasgupta and Clark, 1998). Clee and others (1969) measured both Q_p and the shear-wave quality factor, Q_s, in ice near its melting point.

Attenuation measurements have been made across various depth ranges, with some authors measuring Q over the entire ice column from the spectra of pairs of primary/multiple reflections (e.g. Robin, 1958; Bentley, 1971; Jarvis and King, 1993; Booth and others, 2012). Others have measured Q within narrower depth ranges, either by using strong basal and englacial reflections (e.g. Jarvis and King, 1993; Peters and others, 2012)

or by measuring the amplitude decay of the direct P wave in a vertical seismic profile (Booth and others, 2020). Q has been measured in the uppermost ice of a snow-free glacier (Gusmeroli and others, 2010), and at a single depth at the base of the firn column (Peters, 2009); however little attention has been paid to the depth dependence of attenuation at intermediate depths in the firn column. Measurements of Q are therefore desirable to provide further insight into the structure of the firn itself.

In this study, we use continuously refracted seismic waves to measure the depth dependence of Q_p in the firn column. We use measurements from basal reflection/source ghost pairs and critical refractions to corroborate our results. Q refers to the compressional-wave quality factor unless stated otherwise.

2. Data

2.1. Field site

Korff Ice Rise (KIR) is located in the Weddell Sea region of West Antarctica, surrounded by the Ronne Ice Shelf (Fig. 1). The ice is 530 ± 5 m thick at the divide (the boundary between ice flow directions), with flow velocity <10 m/a (Kingslake and others, 2016; Brisbourne and others, 2019). Seismic data were acquired in January 2015 along a line parallel to the ice divide.

2.2. Surface-source data (acquisitions A1 and A2)

To constrain Q in the uppermost firn, a line of vertically oriented georods (Voigt and others, 2013) was deployed with offset intervals progressively increased: 2.5 m between offsets of 2.5 m and 20 m, 5 m to 50 m and 10 m thereafter to a maximum offset of 390 m. A seismic detonator at the surface was used as the source. We call this acquisition A1; Data are shown in Figure 2a.

To constrain Q deeper in the firn, we use data from a second acquisition, which we call A2: a line of vertically oriented georods, deployed at 10 m offset intervals between 30 m and 980 m. A 150 g
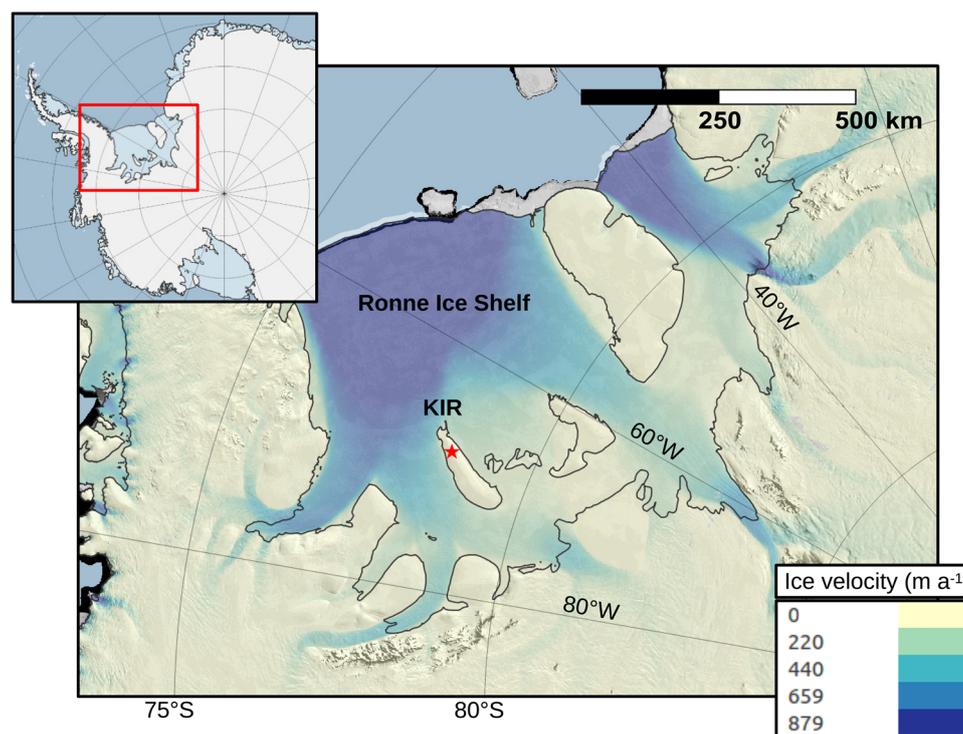
Figure 1. Location of the field site (red star) on Korff Ice Rise (KIR) in the Ronne Ice Shelf. Inset shows the location within Antarctica. MODIS imagery (Scambos and others, 2007) is overlain by MEaSUREs flow velocities (Rignot and others, 2011; Mouginot and others, 2012, 2017; Rignot and others, 2017), accessed through Quantarctica (Matsuoka and others, 2021).
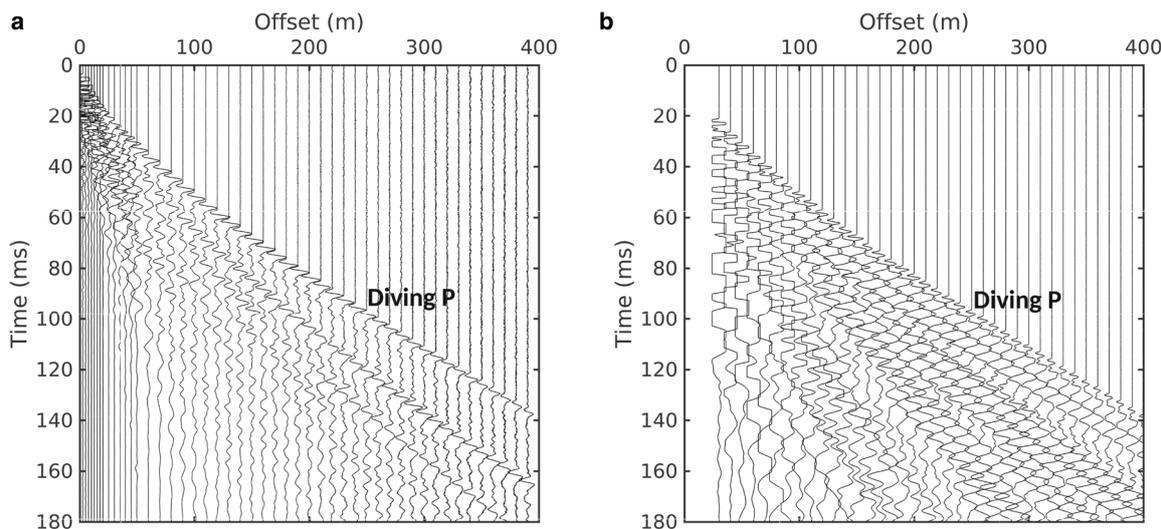
Figure 2. (a) Diving wave first breaks from the expanding spread refraction experiment (acquisition A1), used to constrain v and Q near the surface. Source: seismic detonator at surface. (b) First 400 m of diving wave first breaks from acquisition A2 used for the layer stripping computation. Source: 150 g Pentolite at surface. Traces are normalised in both (a) and (b).

Pentolite source was used, also at the surface, and 2 s of data were recorded with a 16 kHz sampling rate (data are shown in Fig. 2b).

2.3. Buried source data (acquisition B)

In addition to the layouts with the source at the surface, data were acquired from a line of vertically oriented georods at 10 m intervals, installed between 30 m and 1940 m offset, with a 150 g Pentolite source buried in a 20 m deep borehole. These data were recorded with an 8 kHz sampling rate. We call this acquisition B, and use these data to measure Q using the primary, multiple, source ghost and critical refraction. Figure 3 shows primary, source ghost and multiple phases.

A summary of acquisitions A1, A2 and B is given in Table 1. Data will be made available at the UK Polar Data Centre.

3. Methods

The fundamental method we use is the spectral ratio method (Section 3.1), which we apply in different ways to measure Q in various portions of the ice column. The process we present to measure Q vs depth in the firn is layer stripping (Section 3.3).

Layer stripping requires Q at the surface, Q_1, to be constrained independently, so we measure this using direct waves (Section 3.4.1), calling the result Q_{1d}. By initialising the layer stripping process with Q_{1d}, we obtain a full Q profile of the firn.

The other measurements we present corroborate our firn Q results. We measure Q from the surface to the bed, Q_{tot}, using the primary reflection and first multiple (Section 3.2). By combining Q_{tot} with our firn Q profile, we obtain Q in the section between the base of the firn and the bed, Q_{ice}. We compare this to a measurement made in the uppermost solid ice from critically refracted waves, Q_{crit} (Section 3.5). Additionally, we independently measure Q in the upper firn from the source ghosts of primary and first multiple phases, giving the results Q_{1pg} and Q_{1mg} (Section 3.4.2). We compare these to the direct wave result, Q_{1d}.

A summary of each measurement, its depth, acquisition type and offset range is given in Table 2; Figure 4 shows a schematic of the measurements and their depths.

3.1. Spectral ratio method

Seismic attenuation is routinely measured using the spectral ratio method (Teng, 1968; Båth, 1974). The amplitude spectrum $S(f, r)$
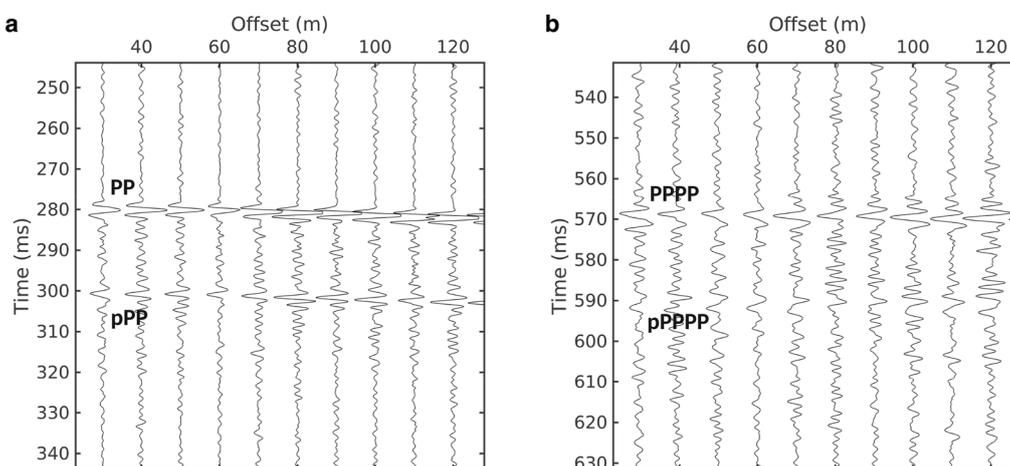

Figure 3. Normal incidence traces from buried source data, acquired in acquisition B. (a) The primary reflection (PP) and its source ghost reflection (pPP) are used to measure Q above the source. (b) The primary and first multiple (PPPP) are used to measure Q from surface to bed. The source ghost (pPPPP) is also present.

Table 1. Summary of acquisition geometries A1, A2 and B

Acquisition name	Source	Sample rate (kHz)	Receiver spread
A1	Seismic detonator at surface	16	Spread from 2.5 m– 390 m; progressively increasing georod intervals: 2.5 m between 2.5 m and 20 m, 5 m between 20 and 50 m, and 10 m between 50 m and 390 m.
A2	150 g Pentolite at surface	16	Offsets from 30 m - 710 m, 10 m georod interval
B	150 g Pentolite buried at 20 m depth	8	Offsets from 30 m–1940 m, 10 m georod interval

Table 2. Summary of the survey layout used for each of the velocity and attenuation measurements

Measurement	Depth (m)	Acquisition	Offset range used
Velocity	$0 - 90$	A1	$0 - 390$ m
Q in uppermost firn from direct waves (Q_{1d})	$0 - 12$	A1	Reference trace at 17.5 m offset; Comparison traces at 30, 35 and 40 m offset.
Q in firn from layer stripping (Q_{2-4})	$27 - 77$	A2	110 m – 710 m
Q in uppermost firn from source ghost Q_{1pg}, Q_{1mg}	$0 - 20$	B	30 m – 140 m (normal incidence traces).
Surface-to-bed Q from primary and multiple (Q_{tot})	$0 - 530$	B	40 m – 140 m (normal incidence traces).
Q at base of firn from critical refraction (Q_{crit})	90	B	990 m – 1460 m
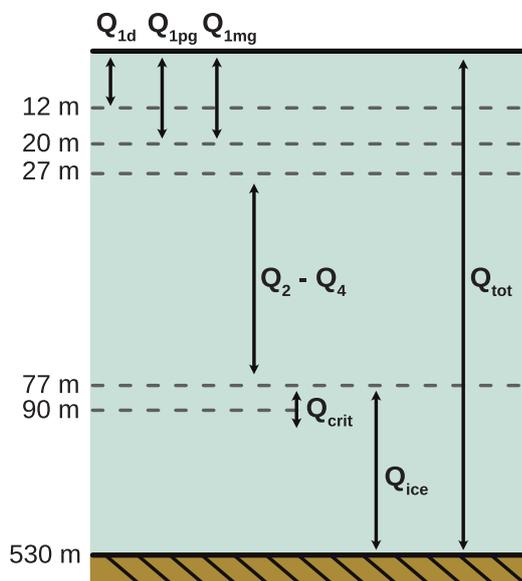
Figure 4. Schematic of measurements made and their depths. Note that depths are not to scale.

of a seismic wavelet of frequency f which has propagated a distance r with no transmission or reflection at interfaces is given by:

$$S(f, r) = S_0(f)G(r)e^{-\alpha(f)r}, \qquad (1)$$

where $S_0(f)$ is the initial spectrum, $G(r)$ describes geometric spreading and a is the attenuation rate, related to Q by $\alpha = \pi f / Qv$ at frequency f and velocity v. The spectral ratio method compares the spectrum $S^A(f)$ of a reference wavelet A to that of a second wavelet B, $S^B(f)$, which travels for an additional time δt. The logarithmic ratio of the spectra is

$$\ln \frac{S^B(f)}{S^A(f)} = \frac{-\pi \delta t}{Q} f + \text{constant} \qquad (2)$$

Linear regression of the spectral ratio's logarithm against frequency allows a measurement of Q to be made from the slope m:

$$m = -\pi \frac{\delta t}{Q} \qquad (3)$$

Figure 5 shows examples of wavelets, their spectra and associated logarithmic spectral ratios used for a calculation of Q in the firn (Section 3.3.1). In all spectral ratio measurements, a bandwidth must be chosen over which the spectral ratios are considered sufficiently linear; m is the curve's gradient within this bandwidth.

We use the common assumption that Q is independent of frequency (Kjartansson, 1979). We assume a low-loss formulation and definition of Q (e.g. O'Connell and Budiansky, 1978; Toverud and Ursin, 2005) and a non-dispersive velocity (Kjartansson, 1979; Liner, 2012); we also assume that Q is isotropic.

Appendix B contains examples of traces, spectra and spectral ratios used for each application of the spectral ratio method.

## 3.2. Surface-to-bed Q measurement (Q_{tot})

A common process for measuring Q to correct for attenuation in seismic reflection studies is to use the spectral ratio of the primary reflection and its multiples (e.g. Booth and others, 2012) with Equation (3). This gives the effective Q from surface to bed, Q_{tot}, which includes the firn and its underlying ice (Fig. 6a). We select non-clipped normal incidence traces from acquisition B for our measurement (Fig. 3), taking incidence angles <10° as normal (Smith, 2007). These wavelets and their spectra are shown in detail in Appendix B.

3.3. Deriving Q in the firn

The spectral ratio method usually measures the difference in frequency content of a propagating wavelet at different locations on an otherwise collinear path. We use a modified process which takes advantage of the firn's continuous velocity gradient and the resulting diving wave paths (e.g. Hepburn, 2016; Alsuleiman, 2018; Crane and others, 2018). We use Wiechert–Herglotz inversion to obtain a velocity model (WHI: Herglotz, 1907; Wiechert, 1910; Slichter, 1932); WHI has been widely used for application to firn (e.g. Kirchner and Bentley, 1990; Jarvis and King, 1993; King and Jarvis, 2007; Schlegel and others, 2019; Hollmann and others, 2021).

3.3.1. Layer stripping
For the purposes of this method, we represent the firn column as a sequence of layers of uniform Q; the stated quality factor for an individual quasi-layer describes the aggregated effect of attenuation over a defined vertical interval. Layer stripping is an established technique in seismic tomography and attenuation analysis
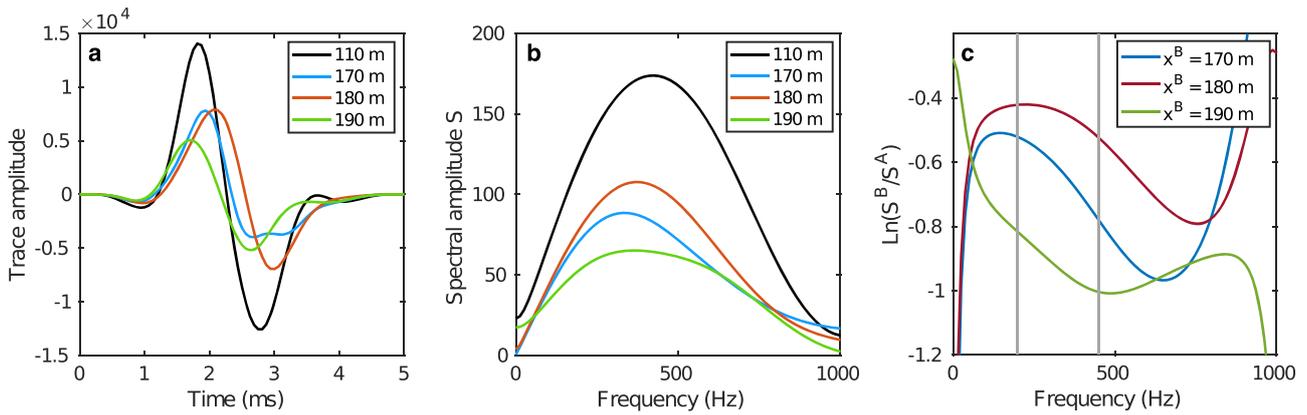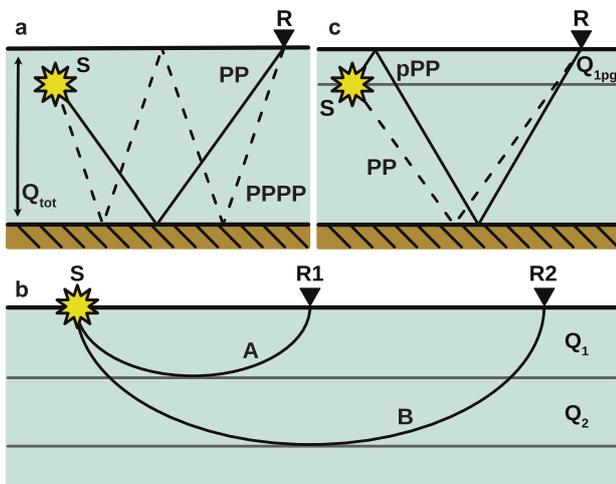
Figure 5. (a) Wavelets and (b) spectra of diving waves used for the calculation of Q in the second layer of the firn, Q_2. Legends (a) and (b) indicate the source-receiver offsets of the traces and spectra. The trace at 110 m offset (black) is used as the reference trace, with spectrum S^A. (c) Logarithmic spectral ratios used for the calculation. The comparison trace has spectrum S^B and source-receiver offset x^B. The spectral ratios are considered to be sufficiently linear within the chosen bandwidth of $200 - 450$ Hz, indicated by the grey vertical lines.

(e.g. Quan and Harris, 1997; Yilmaz, 2001), and it is the process by which we calculate the quality factor of an individual quasi-layer in the firn. This combines spectral ratio measurements of wavelets passing through that layer with an evaluation of the cumulative attenuation through all overlying layers.

Figure 6b shows two diving waves A and B arriving at receivers R1 and R2, having passed through different portions of the firn column. We trace these rays to find their depths of maximum penetration and interpret layers of uniform Q between these depths, discretising what we assume to be a gradual change in attenuative properties with depth as the firn compacts. The attenuated time t^*, defined as $t^* = t/Q$, is cumulative along each ray (Carpenter and others, 1966); i.e. for a ray which travels through n layers:

$$t^*_{ray} = \sum_{i=1}^{n} t^*_i = \sum_{i=1}^{n} \frac{t_i}{Q_i} \qquad (4)$$

where t_i is the time a ray spends in layer i, and Q_i is the quality factor in that layer. A wavelet's attenuated time is not measured directly; however, the difference in t^* between two wavelets, δt^*, can be measured from their spectral ratio gradient $m = -\pi \delta t^*$. Ray-tracing is used to determine the time each ray spends in each layer; combined with the measured spectral ratio gradients, this is used to calculate Q in each successive layer. Q_n in layer n is calculated using the spectral ratio gradient of two rays A and B, which penetrate to the bottom of layers $n-1$ and n, respectively:

$$Q_n = t^B_n \left[\frac{-m^{B,A}}{\pi} + \sum_{i=1}^{n-1} \frac{t^A_i - t^B_i}{Q_i} \right]^{-1} \qquad (5)$$

Here, the superscripts denote the ray and the subscripts denote the layer; i.e., Q_n is the quality factor in layer n, t^A_i is the time ray A spends in layer i, and $m^{B,A}$ is the gradient of the spectral ratio $S^B(f)/S^A(f)$. A derivation of this equation is given in Appendix A.

It is apparent from Equation (5) that the calculation of Q in each successive layer depends on the calculation of Q in all of the shallower layers. This process requires Q in the uppermost layer to be known before the others can be calculated; we measure this using near-offset direct waves (Section 3.4.1).

In principle, an attenuation-depth profile as smooth as the velocity-depth profile could be constructed using each successive offset pair; however, in practice, a vertical interval must be thick and/or attenuative enough that its Q contribution is detectable above noise. To obtain more robust results, we use clusters of three adjacent traces which, taken together, define the layer boundaries (Fig. 6b), calculating and averaging nine Q_i^{-1} results for each layer. Figure 5 shows examples of traces, spectra and spectral ratios for the calculation of Q in the second layer. We choose traces and bandwidths based on inspection of individual spectra, avoiding traces with notched or unstable spectra.

We construct a four-layer Q_p model based on available stable spectra with sufficiently large offset differences for a reliable measurement to be made, using data from the line of georods offset at 10 m intervals with a 150 g Pentolite source at the surface (acquisition A2).

Figure 6. (a) The primary reflection (solid, PP) and first multiple (dashed, PPPP) are used to measure effective Q across the glacier's entire depth, Q_{tot}. (b) Diving waves travelling between source S and receivers R1, R2. We define layers of constant Q and take the bottoming depth of the rays to be the layer boundaries. (c) The spectral ratio of the primary reflection (dotted, PP) and source ghost (solid, pPP) can be used to calculate Q in the uppermost layer, above a buried source. Note that this is schematic, and (a) and (c) do not show refraction of ray paths due to the firn's velocity gradient.

3.3.2. Stochastic error analysis

We estimate uncertainties in velocities by applying Gaussian perturbations to wavelet travel times before Wiechert–Herglotz inversion, repeating the process to obtain distributions of velocities as a function of depth. We then calculate the mean and standard deviation of the output distributions to obtain velocity-depth curves.

To estimate the propagation of errors through the layer stripping process, we implement a stochastic framework of error

analysis. After Q_i is calculated for layer i, a Gaussian perturbation is applied to Q_i^{-1} consistent with the uncertainty on the spectral ratio slope, and this perturbed Q_i is used to calculate the Q_{i+1} of the next layer. We repeat this process 1000 times to obtain a large number of credible models to analyse statistically. In order to ensure that each generated $Q(z)$ model is physically plausible, we assume two conditions and accept only models which satisfy these. We require that Q increases with depth (i.e., $Q_{i+1} > Q_i$), and that $Q > 0$ always. We assume that the uncertainty is dominated by the spectral ratios and that the uncertainty from the travel-time measurement is comparatively small. Although these assumptions do not allow all theoretically possible results, we consider them necessary in order to obtain a large enough number of usable models from which statistics can be robustly calculated, given our computational constraints. All statistics are computed from distributions of the quantity $\rho = Q^{-1}$, and results and uncertainties are quoted as the mean and standard deviation of the output distributions. The uncertainty in Q is then derived from $\epsilon_Q = \epsilon_\rho/\rho^2$, where ϵ_Q is the error in Q and ϵ_ρ is the error in ρ (Topping, 1972).

3.4. Constraining near-surface Q

$Q(z)$ profiles output from layer stripping reveal relative variations, but evaluating absolute values requires Q in the shallowest layer, Q_1, to be constrained. We initialise our layer stripping process with a measurement of Q_1 from direct waves, which we call Q_{1d}, and use measurements from primary and multiple source ghosts (Q_{1pg} and Q_{1mg}) to support this result.

3.4.1. Direct wave measurement, Q_{1d}
Measuring Q_1 from direct waves enables its constraint without the use of a buried source. Approximating near-offset diving waves as direct waves, we calculate Q_{1d} using their spectral ratios. The layer thickness d is the maximum thickness of the ray's first Fresnel volume, given by

$$d(x) = \sqrt{3\lambda x}/4, \tag{6}$$

where λ is the wavelength and x the source-receiver offset of the further offset ray in the pair (Spetzler and Snieder, 2004; Gusmeroli and others, 2010). For the direct wave calculation, we use data acquired with a seismic detonator as source, which for our selected rays gives Q_{1d} in a layer 12 m thick. We initialise our layer stripping computation with Q_{1d}. For layer stripping, we use the nearest-offset non-clipped traces from acquisition A1; these rays reach 27 m depth, requiring that we assume $Q_1 = Q_{1d}$ to 27 m.

3.4.2. Source ghost measurement, Q_{1pg}, Q_{1mg}
These results are used to corroborate the direct wave measurement of Q_{1d}. We acquired data with a buried source (20 m depth, acquisition B) which generates a discrete source ghost. We use these data to provide an independent measurement of Q in the upper 20 m. Figure 6c shows the ray paths of the primary reflection and its source ghost. The spectral ratio gradient for these two wavelets at normal incidence is used with Equation (3) to calculate Q, which we call Q_{1pg}. The traces used to calculate Q_{1pg} are shown in Figure 3a.

Shown in Figure 3b are the normal incidence first multiple (PPPP) and its source ghost (pPPPP). Measuring Q using these wavelets also gives Q in the firn above the shot, which we call Q_{1mg}. Ideally, we would expect Q_{1pg} and Q_{1mg} to be equal.

3.5. Constraining Q in the ice from multiples and critical refractions

3.5.1. Critical refraction, Q_{crit}
To validate the layer stripping approach to calculating Q, we make an independent measurement of Q in the uppermost solid ice, Q_{crit}, using critically refracted waves (Peters, 2009). Critical refractions occur at the point at which seismic velocity stops increasing. At this depth, Q_{crit} can be straightforwardly measured using the spectral ratio of two critically refracted arrivals and Equation (3). For this measurement, we use data with a 150 g buried Pentolite shot (acquisition B). We calculate the thickness of this quasi-layer using Equation (6).

3.5.2. Combining Q_{tot} with a firn-Q model
We combine our layer-stripping measurement with our measurement of Q_{tot} to provide an estimate of Q between the base of the firn and the bed, Q_{ice}:

$$Q_{ice} = t_{ice} \left[\frac{t_{tot}}{Q_{tot}} - \sum^{firn} \frac{t_i}{Q_i} \right]^{-1}. \tag{7}$$

Here, t_{ice} is the travel time of a normal-incidence reflection between the base of the firn and the bed, t_{tot} is the travel time between surface and bed, t_i is the travel time in a layer i of the firn, and Q_i is the quality factor of that layer. Since the measurement of Q_{ice} is dependent on layer stripping, it is possible to validate the layer stripping process by evaluating the consistency of Q_{crit} and Q_{ice}.

4. Results

WHI yields the velocity-depth model shown in Figure 7a. The P-wave velocity increases with depth from 1200 ± 340 m s^{-1} at 1 m depth to 3779 ± 30 m s^{-1} at 90 m depth.

The surface-to-bed Q is $Q_{tot} = 250 \pm 100$ measured using the primary and first multiple. The direct wave measurement of Q_1 gives $Q_{1d} = 56 \pm 23$ in the uppermost 12 m of firn. From the primary reflection/ghost measurement, we find $Q_{1pg} = 53 \pm 20$ for the uppermost 20 m, and from the first multiple/ghost, we find $Q_{1mg} = 53 \pm 24$ for the uppermost 20 m.

The results of our layer stripping computation in combination with stochastic error analysis are shown in Figure 7b, which shows Q increasing to 570 ± 450 between 55 and 77 m depth. Table 3 presents the Q model resulting from the layer stripping process.

By measuring Q at the critical refraction, we obtain $Q = 640 \pm 400$ at 90 ± 14 m. This is indicated in Figure 7b by the dashed red line and shaded red area.

For a normal incidence reflection, our layered Q model, when combined with Q_{tot}, implies that for the entire ice column at depths greater than 77 m, $Q_{ice} = 400 \pm 310$. This result is dependent on layer stripping and is shown in Figure 7b as the deepest layer with a dotted blue line, with errors indicated by the shaded area. Table 4 summarises all Q measurements which are independent of layer stripping.

5. Discussion

We have shown an effective process of deriving the velocity and attenuation profiles through firn and ice, including a robust evaluation of uncertainties. Comparison of Q results obtained from layer stripping with independent measurements at similar depths shows consistency between methods. Our measurements of $Q_4 = 570 \pm 450$, $Q_{ice} = 400 \pm 310$ and $Q_{crit} = 640 \pm 400$ agree with each other within uncertainties, supporting the use of the layer stripping process. The large uncertainties in our results arise from
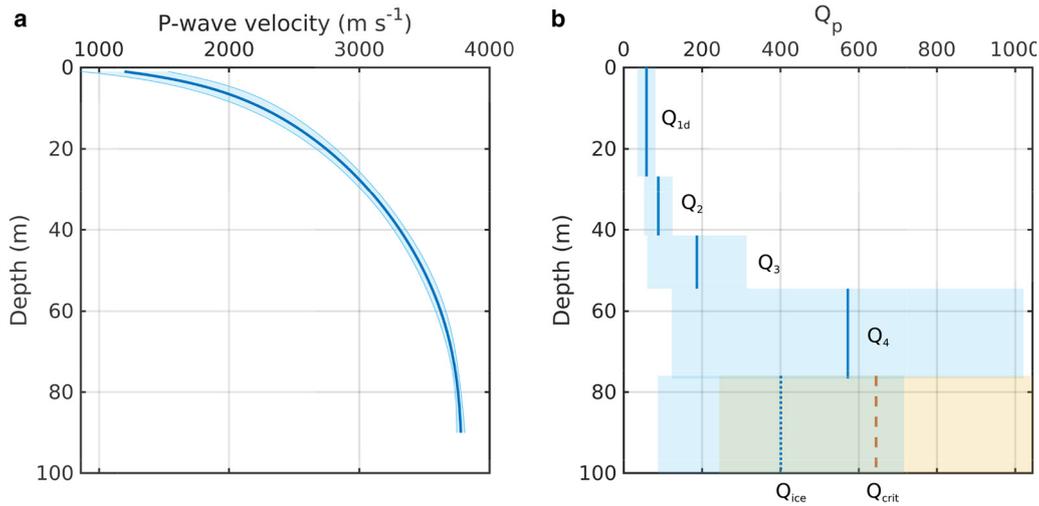
Figure 7. (a) Results from Wiechert–Herglotz inversion, showing the depth dependence of seismic velocity. (b) Dependence of quality factor Q on depth z. Q_{1d} is measured from direct waves and assumed constant to 27 m. $Q_2 - Q_4$ result from the layer stripping process. The blue dotted line shows Q_{ice} resulting from combining the Q_{tot} measurement with the layered model $Q_1 - Q_4$. The red dashed line shows Q at the base of the firn, Q_{crit}, measured using the critical refraction. Shaded areas represent uncertainties.

Table 3. Q_p model from the layer stripping process, shown in Figure 7b

Layer	Depth range (m)	Q
Q_1 (from Q_{1d})	$0 - 27$	56 ± 23
Q_2	$27 - 41$	89 ± 36
Q_3	$41 - 55$	190 ± 130
Q_4	$55 - 77$	570 ± 450
Q_{ice} from layer stripping/multiple	$77 - 530$	400 ± 310

For the first layer, $0 - 27$ m, we take $Q_1 = Q_{1d}$ from the direct wave measurement.

Table 4. Summary of measurements independent of layer stripping

Measurement	Depth range (m)	Q
Q_{tot} from primary/first multiple	$0 - 530$	250 ± 100
Surface Q from direct wave, Q_{1d}	$0 - 12$	56 ± 23
Surface Q from primary source ghost, Q_{1pg}	$0 - 20$	53 ± 20
Surface Q from first multiple source ghost, Q_{1mg}	$0 - 20$	53 ± 24
Uppermost solid ice Q from critical refraction, Q_{crit}	90	640 ± 400

the variability in spectral ratio slope which propagates through the layer stripping process to Q_4 and Q_{ice}. Furthermore, to conform with our stochastic error analysis, our quoted errors on Q are derived from the standard deviations of Q^{-1}; other authors (e.g. Gusmeroli and others, 2010) quote standard errors, which makes direct comparison inappropriate. Fundamentally, the uncertainties are determined by the bandwidth and signal-to-noise ratio of the diving-wave arrivals, which could be improved in many ways - for example, by ensuring excellent receiver coupling.

In the shallow firn, our measurements of $Q_{1d} = 56 \pm 23$, $Q_{1pg} = 53 \pm 20$, and $Q_{1mg} = 53 \pm 24$ agree closely, despite the fact that the direct wave samples the top 12 m (Q_{1d}) and the source ghost samples the top 20 m of firn (Q_{1pg}, Q_{1mg}). This is suggestive of a shallow Q gradient in the upper firn.

A key motivation for measuring Q in the firn is the need to compensate for Q losses when the amplitude of seismic waves is of interest, for example when using amplitude-versus-offset (AVO) analysis to identify a subglacial material (e.g. Peters and others, 2008; Booth and others, 2012). We assess the impact of
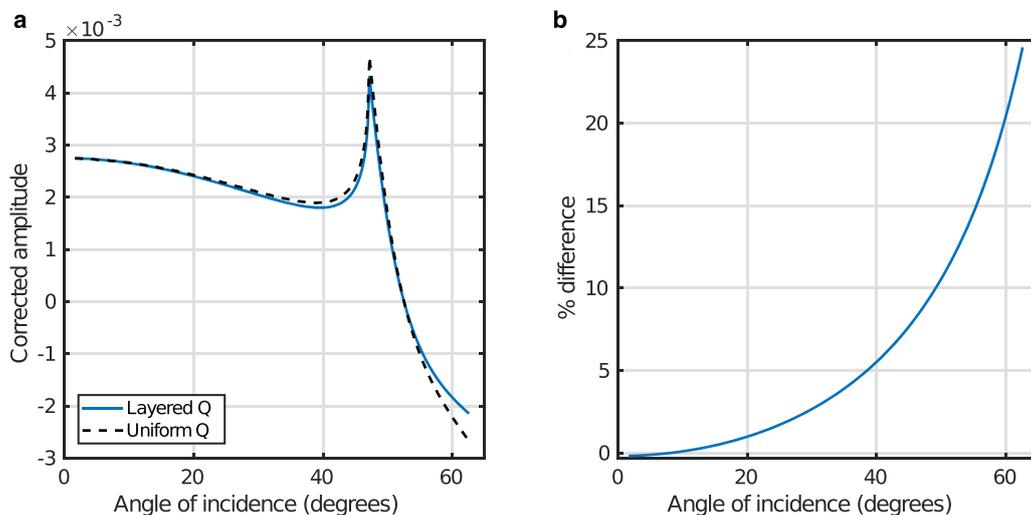
Figure 8. (a) Bed reflectivities obtained from synthetic amplitude-versus-offset (AVO) data simulating a reflection from an ice-bedrock interface with a Korff-like geometry, correcting for attenuation with a layered Q model (solid blue line), and a uniform-Q assumption (dashed black line). Data are not corrected for synthetic source amplitude and the y-axis is consequently multiplied by a constant. (b) Difference between layered-Q-corrected and uniform-Q-corrected AVO curves (%).

a layered Q model by considering what difference such a model would make to an AVO measurement versus a model which assumes a uniform Q_{tot} throughout the whole glacier. We produce a synthetic AVO gather of a reflection from 530 m thick ice over bedrock, dominant frequency 200 Hz, which incorporates our detailed firn-Q model and velocity model. We then pick the amplitudes, and recalculate the bed reflection coefficient using (a) our detailed Q model including Q_{ice}, and (b) the assumption that $Q = 250$ everywhere. We correct the amplitudes for a single frequency, $f = 200$ Hz. Figure 8a shows the two corrected reflectivity curves, and Figure 8b shows the percentage difference between the layered-Q corrected and uniform-Q corrected curves. The difference is small compared with typical signal-to-noise ratios at angles <50°, rising to > 10% at angles >50°. Layer stripping could therefore in theory provide a small benefit to AVO surveys which have very high-quality and wide-angle data. However, for typical glaciological AVO experiments layer-stripping will provide minimal benefits if Q can be measured using the primary and first multiple.

There are circumstances in which it would be preferable to choose a layer stripping measurement over a multiple-based one. First, for seismic experiments studying the firn itself, a measurement of Q in the firn is necessary, as clearly it is not valid to assume that Q at shallow depths is the same as the effective Q that would be measured using multiples. Second, thin layering at the ice-bed interface (Booth and others, 2012) can cause interference effects which change the apparent amplitudes of the primaries and multiples, making a multiple-based measurement inappropriate where a thinly layered bed is suspected. Third, multiples are not always clearly visible in a seismic dataset (e.g. Dow and others, 2013; Muto and others, 2019); in such a case Q would need to be estimated by layer stripping.

Our method has potential for improvement. A more detailed model could be produced if more closely spaced, or even all, traces were used, resulting in a model with very thin layers and providing a more accurate representation of the continuous nature of firn transformation; however, this would require an extremely high signal-to-noise ratio that was not achieved with our dataset. In principle, layer stripping could be used to measure the shear-wave quality factor; the acquisition would need to be designed with this in mind, with an S-wave source and closely spaced receivers at near offsets. In addition to our P-wave data, we acquired S-wave data using a 600 g Pentolite source; however the size of the source needed to generate S-waves caused a high degree of clipping and contamination with P-waves, rendering a Q-analysis impossible. In the future, layer stripping could be combined with measurements relying on englacial reflections (e.g. Peters and others, 2012) in order to build up a more comprehensive englacial Q-profile; this could be supplemented by a dedicated microspread to resolve detail at very shallow depths (e.g. Gusmeroli and others, 2010). For complex firn structures such as those with ice lenses or hoar frost layers, WHI fails to capture the true velocity-depth relationship, and more advanced inversion methods such as full waveform inversion could be used to jointly invert for velocity and attenuation structures (e.g. Pearce and others, 2023a, 2023b).

6. Conclusions

We have demonstrated a novel application of the spectral ratio method for the measurement of the seismic quality factor Q in firn, and applied the method to data from Korff Ice Rise in West Antarctica. We have therefore been able to resolve the compressional-wave attenuative structure of firn in greater detail than has previously been possible. We have combined our layer stripping method with a stochastic method of error propagation. Our results show Q increasing from 56 ± 23 in the uppermost 12

m to 570 ± 450 between 55 and 77 m depth. We corroborate results from layer stripping with independent measurements using critically refracted waves, the source ghost and primary/multiple reflections. Using the primary reflection and source ghost shows $Q = 53 \pm 20$ in the uppermost 20 m of firn, and using critically refracted waves shows $Q = 640 \pm 400$ at 90 m depth. The layer stripping process can be used for seismic studies of firn or seismic reflection studies where conventional methods of measuring Q are not possible. Our results provide a fuller characterisation of firn's seismic properties than has previously been shown, and our methods will aid future seismic investigations of glaciological targets.

References

Aki K and Richards PG (2002) *Quantitative Seismology*. Sausalito, CA, USA: University Science Books.

Alley RB, Spencer MK and Anandakrishnan S (2007) Ice-sheet mass balance: assessment, attribution and prognosis. *Annals of Glaciology* **46**, 1–7. doi: 10. 3189/172756407782871738

Alsuleiman A (2018) *Measuring seismic attenuation for the firn layer in Antarctica*. Unpublished BSc. Geophysical Sciences dissertation, School of Earth and Environment, University of Leeds.

Båth M (1974) *Developments in Solid Earth Geophysics: Spectral Analysis in Geophysics*. Amsterdam: Elsevier Scientific Publishing Company.

Bentley CR (1971) Seismic Evidence for Moraine within the Basal Antarctic Ice Sheet. In Crary A ed. *Antarctic Research Series*. Washington, D. C: American Geophysical Union, pp. 89–129.

Bentley CR and Kohnen H (1976) Seismic refraction measurements of internal friction in Antarctic ice. *Journal of Geophysical Research* **81**(8), 1519–1526. doi: 10.1029/JB081i008p01519

Booth AD and 6 others (2012) Thin-layer effects in glaciological seismic amplitude-versus-angle (AVA) analysis: implications for characterising a subglacial till unit, Russell Glacier, West Greenland. *The Cryosphere* **6**(4), 909–922. doi: 10.5194/tc-6-909-2012

Booth AD and 8 others (2020) Distributed acoustic sensing of seismic properties in a borehole drilled on a fast-flowing Greenlandic outlet glacier. *Geophysical Research Letters* **47**(13), e2020GL088148. doi: 10.1029/2020GL088148

Booth AD, Emir E and Diez A (2016) Approximations to seismic AVA responses: Validity and potential in glaciological applications. *Geophysics* **81**(1), WA1–WA11. doi: 10.1190/geo2015-0187.1

Brisbourne AM and 5 others (2019) Constraining recent ice flow history at Korff Ice Rise, West Antarctica, using radar and seismic measurements of ice fabric. *Journal of Geophysical Research: Earth Surface* **124**(1), 175–194. doi: 10.1029/2018JF004776

Carpenter EW, Bullard EC and Penney WG (1966) A quantitative evaluation of teleseismic explosion records. *Proceedings of the Royal Society of London. Series A. Mathematical and Physical Sciences* **290**(1422), 396–407. doi: 10. 1098/rspa.1966.0058

Clee TE, Savage JC and Neave KG (1969) Internal friction in ice near its melting point. *Journal of Geophysical Research* **74**(4), 973–980. doi: 10.1029/JB074i004p00973

Crane JM, Lorenzo JM, Shen J and White CD (2018) The competing effects of stress and water saturation on *in situ* Q for shallow (< 1 m), unconsolidated sand, evaluated with a modified spectral ratio method. *Near Surface Geophysics* **16**(2), 104–117. doi: 10.3997/1873-0604.2017048

Dasgupta R and Clark RA (1998) Estimation of Q from surface seismic reflection data. *Geophysics* **63**(6), 2120–2128. doi: 10.1190/1.1444505

Dow CF and 5 others (2013) Seismic evidence of mechanically weak sediments underlying Russell Glacier, West Greenland. *Annals of Glaciology* **54**(64), 135–141. doi: 10.3189/2013AoG64A032

Gusmeroli A and 5 others (2010) Seismic wave attenuation in the uppermost glacier ice of Storglaciären, Sweden. *Journal of Glaciology* **56**(196), 249–256. doi: 10.3189/002214310791968485

Hepburn D (2016) *Estimation of the seismic attenuation in firn through use of the Wiechert–Herglotz Inversion and spectral ratio methods.* Unpublished MSc. Exploration Geophysics dissertation, School of Earth and Environment, University of Leeds.

Herglotz G (1907) Über das Benndorfsche problem der fortpflanzungsgeschwindigkeit der erdbebenstrahlen (on the Benndorf problem of propagation velocity of earthquake rays). *Zeitschrift für Geophysik* **8**, 145–147.

Hollmann H, Treverrow A, Peters LE, Reading AM and Kulessa B (2021) Seismic observations of a complex firn structure across the Amery Ice Shelf, East Antarctica. *Journal of Glaciology* **67**(265), 777–787. doi: 10.1017/jog.2021.21

Horgan HJ and 7 others (2021) Grounding zone subglacial properties from calibrated active-source seismic methods. *The Cryosphere* **15**(4), 1863–1880. doi: 10.5194/tc-15-1863-2021

Horgan HJ, Anandakrishnan S, Alley RB, Burkett PG and Peters LE (2011) Englacial seismic reflectivity: imaging crystal-orientation fabric in West Antarctica. *Journal of Glaciology* **57**(204), 639–650. doi: 10.3189/002214311797409686

Hubbard B and 12 others (2016) Massive subsurface ice formed by refreezing of ice-shelf melt ponds. *Nature Communications* **7**(1), 11897. doi: 10.1038/ncomms11897

Jarvis E and King E (1993) The seismic wavefield recorded on an Antarctic ice shelf. *Journal of Seismic Exploration* **2**, 69–86.

King EC and Jarvis EP (2007) Use of shear waves to measure Poisson's ratio in polar firn. *Journal of Environmental and Engineering Geophysics* **12**(1), 15–21. doi: 10.2113/JEEG12.1.15

Kingslake J, Martín C, Arthern RJ, Corr HFJ and King EC (2016) Ice-flow reorganization in West Antarctica 2.5 kyr ago dated using radar-derived englacial flow velocities. *Geophysical Research Letters* **43**(17), 9103–9112. doi: 10.1002/2016GL070278

Kirchner JF and Bentley CR (1990) RIGGS III: Seismic short-refraction studies using an analytical curve-fitting technique. In Bentley CR and Hayes DE (eds.), *Antarctic Research Series*. Washington, D. C: American Geophysical Union, pp. 109–126.

Kjartansson E (1979) Constant *Q* -wave propagation and attenuation. *Journal of Geophysical Research* **84**(B9), 4737. doi: 10.1029/JB084iB09p04737

Kohnen H (1972) Über die beziehung zwischen seismischen geschwindigkeiten und der dichte in firn und eis. *Zeitschrift für Geophysik* **38**(5), 925–935.

Kuipers Munneke P, Ligtenberg SR, Van Den Broeke MR and Vaughan DG (2014) Firn air depletion as a precursor of Antarctic ice-shelf collapse. *Journal of Glaciology* **60**(220), 205–214. doi: 10.3189/2014JoG13J183

Kulessa B and 10 others (2019) Seawater softening of suture zones inhibits fracture propagation in Antarctic ice shelves. *Nature Communications* **10**(1), 5491. doi: 10.1038/s41467-019-13539-x

Kuroiwa D (1964) Internal friction of ice. III : The internal friction of natural glacier ice. *Contributions from the Institute of Low Temperature Science* **18**, 49–62.

Liner CL (2012) *Elements of seismic dispersion: A somewhat practical guide to frequency-dependent phenomena.* Society of Exploration Geophysicists, DISC Series 15.

Matsuoka K and 21 others (2021) Quantarctica, an integrated mapping environment for Antarctica, the Southern Ocean, and sub-Antarctic islands. *Environmental Modelling & Software* **140**, 105015. doi: 10.1016/j.envsoft.2021.105015

Mouginot J, Rignot E, Scheuchl B and Millan R (2017) Comprehensive annual ice sheet velocity mapping using Landsat-8, Sentinel-1, and RADARSAT-2 data. *Remote Sensing* **9**(4), 364. doi: 10.3390/rs9040364

Mouginot J, Scheuchl B and Rignot E (2012) Mapping of ice motion in Antarctica using synthetic-aperture radar data. *Remote Sensing* **4**(9), 2753–2767. doi: 10.3390/rs4092753

Muto A and 7 others (2019) Relating bed character and subglacial morphology using seismic data from Thwaites Glacier, West Antarctica. *Earth and Planetary Science Letters* **507**, 199–206. doi: 10.1016/j.epsl.2018.12.008

O'Connell RJ and Budiansky B (1978) Measures of dissipation in viscoelastic media. *Geophysical Research Letters* **5**(1), 5–8. doi: 10.1029/GL005i001p00005

O'Doherty RF and Anstey NA (1971) Reflections on amplitudes. *Geophysical Prospecting* **19**(3), 430–458. doi: 10.1111/j.1365-2478.1971.tb00610.x

Pearce E and 7 others (2023a) Characterising ice slabs in firn using seismic full waveform inversion, a sensitivity study. *Journal of Glaciology*, FirstView, 1–15. doi:10.1017/jog.2023.30

Pearce E and 7 others (2023b) A synthetic study of acoustic full waveform inversion to improve seismic modelling of firn. *Annals of Glaciology* **63**(87-89), 44–48. doi:10.1017/aog.2023.10

Peters LE and 5 others (2008) Seismic detection of a subglacial lake near the South Pole, Antarctica. *Geophysical Research Letters* **35**(23), L23501. doi: 10.1029/2008GL035704

Peters LE (2009) *A seismic investigation of basal conditions in glaciated regions.* Unpublished PhD thesis, Pennsylvania State University Graduate School.

Peters LE, Anandakrishnan S, Alley RB and Smith AM (2007) Extensive storage of basal meltwater in the onset region of a major West Antarctic ice stream. *Geology* **35**(3), 251. doi: 10.1130/G23222A.1

Peters LE, Anandakrishnan S, Alley RB and Voigt DE (2012) Seismic attenuation in glacial ice: A proxy for englacial temperature. *Journal of Geophysical Research: Earth Surface* **117**(F2), F02008. doi: 10.1029/2011JF002201

Prasad M and Meissner R (1992) Attenuation mechanisms in sands: Laboratory versus theoretical (Biot) data. *Geophysics* **57**(5), 710–719. doi: 10.1190/1.1443284

Quan Y and Harris JM (1997) Seismic attenuation tomography using the frequency shift method. *Geophysics* **62**(3), 895–905. doi: 10.1190/1.1444197

Rignot E, Mouginot J and Scheuchl B (2011) Ice flow of the Antarctic Ice Sheet. *Science* **333**(6048), 1427–1430. doi: 10.1126/science.1208336

Rignot E, Mouginot J and Scheuchl B (2017) MEaSUREs InSAR-based Antarctica ice velocity map, version 2.

Rist MA and 5 others (1996) Experimental fracture and mechanical properties of Antarctic ice: preliminary results. *Annals of Glaciology* **23**, 284–292. doi: 10.3189/S0260305500013550

Robin G (1958) Glaciology III: Seismic shooting and related investigations. *Norwegian–British–Swedish Antarctic Expedition, 1949–52, Scientific Results*, Vol. 5. Oslo: Norsk Polarinstitutt.

Scambos T, Haran T, Fahnestock M, Painter T and Bohlander J (2007) MODIS-based mosaic of Antarctica (MOA) data sets: Continent-wide surface morphology and snow grain size. *Remote Sensing of Environment* **111**(2), 242–257. doi: 10.1016/j.rse.2006.12.020

Schlegel R and 8 others (2019) Comparison of elastic moduli from seismic diving-wave and ice-core microstructure analysis in Antarctic polar firn. *Annals of Glaciology* **60**(79), 220–230. doi: 10.1017/aog.2019.10

Schoenberger M and Levin FK (1974) Apparent attenuation due to intrabed multiples. *Geophysics* **39**(3), 278–291. doi: 10.1190/1.1440427

Sheriff RE and Geldart LP (1995) *Exploration Seismology.* Cambridge, UK: Cambridge University Press.

Slichter LB (1932) The theory of the interpretation of seismic travel-time curves in horizontal structures. *Physics* **3**(6), 273–295. doi: 10.1063/1.1745133

Smith AM (1997) Basal conditions on Rutford Ice Stream, West Antarctica, from seismic observations. *Journal of Geophysical Research: Solid Earth* **102**(B1), 543–552. doi: 10.1029/96JB02933

Smith AM (2007) Subglacial bed properties from normal-incidence seismic reflection data. *Journal of Environmental and Engineering Geophysics* **12**(1), 3–13. doi: 10.2113/JEEG12.1.3

Spetzler J and Snieder R (2004) The Fresnel volume and transmitted waves. *Geophysics* **69**(3), 653–663. doi: 10.1190/1.1759451

Teng TL (1968) Attenuation of body waves and the Q structure of the mantle. *Journal of Geophysical Research (1896–1977)* **73**(6), 2195–2208. doi:10.1029/JB073i006p02195

Topping J (1972) *Errors of Observation and Their Treatment.* 4th Ed. London: Chapman and Hall Science paper back.

Toverud T and Ursin B (2005) Comparison of seismic attenuation models using zero-offset vertical seismic profiling (VSP) data. *Geophysics* **70**(2), F17–F25. doi: 10.1190/1.1884827

Voigt DE, Peters LE and Anandakrishnan S (2013) 'Georods': the development of a four-element geophone for improved seismic imaging of glaciers and ice sheets. *Annals of Glaciology* **54**(64), 142–148. doi: 10.3189/2013AoG64A432

Wiechert E (1910) Bestimmung des weges der Erdbebenwellen im Erdinnern. I. theoretisches (Raypath determination of earthquakes waves in the Earth's interior, I. theory). *Physikalische Zeitschrift* **11**, 294–304.

Wingham DJ (2000) Small fluctuations in the density and thickness of a dry firn column. *Journal of Glaciology* **46**(154), 399–411. doi: 10.3189/172756500781833089

Yilmaz Ö (2001) *Seismic Data Analysis: Processing, Inversion and Interpretation of Seismic Data.* Houston, Texas: Society of Exploration Geophysicists.

Appendix A. Derivation

This is a derivation of Equation (5) seen in the main text. Here superscripts denote rays, and subscripts denote quasi-layers in the firn; e.g. t_2^B is the time ray B spends in layer 2, and Q_2 is the quality factor in that layer. m^B, A is the gradient obtained from the logarithm of the spectral ratio $S^B(f)/S^B(A)$, where $S^B(f)$ is the spectrum of a wavelet following the path of ray B, and $S^A(f)$ is the spectrum of a wavelet following the path of ray A. Figure 6b shows two rays A and B, which reach the bottom of firn quasi-layers 1 and 2, with quality factors Q_1 and Q_2, respectively. These rays would be used to calculate Q in the interval between their maximum penetration depths, i.e. Q_2. The difference in their attenuated times is:

$$
\begin{aligned}
\delta t^{*B,A} &= t^{*B} - t^{*A} \\
&= \left(\frac{t_1^B}{Q_1} + \frac{t_2^B}{Q_2} \right) - \frac{t_1^A}{Q_1}.
\end{aligned}
\tag{A.1}
$$

Assuming Q_1 is known, rearranging for Q_2 gives:

$$
Q_2 = t_2^B \left[\delta t^{*B,A} + \frac{t_1^A - t_1^B}{Q_1} \right]^{-1}
\tag{A.2}
$$

where $\delta t^{\star B,A}$ is computed from the spectral ratio gradient $m = -\pi \delta t^*$. Consider a ray C which penetrates to the base of a third layer; by a similar argument,

$$
Q_3 = t_3^C \left[\delta t^{*C,B} + \frac{t_1^B - t_1^C}{Q_1} + \frac{t_2^B - t_2^C}{Q_2} \right]^{-1}
\tag{A.3}
$$

To calculate Q_n in an arbitrary layer n, we would use the spectral ratio gradient calculated from two rays X and Y, one of which (Y) has penetrated to the base of layer n, and one of which (X) has penetrated to the base of layer $n-1$. By extension of Equation (A.3), Q_n is:

$$
Q_n = t_n^Y \left[\frac{m^{Y,X}}{-\pi} + \sum_{i=1}^{n-1} \frac{t_i^X - t_i^Y}{Q_i} \right]^{-1}.
\tag{A.4}
$$

Appendix B. Data examples

Here we show examples of the wavelets, spectral amplitudes and spectral ratios relied upon for each of our measurements. In each figure, the legend indicates the source-receiver offsets of the traces used. In spectral ratio plots, the vertical grey lines indicate the bandwidth over which the gradient is measured. Figure 9 shows the relevant wavelets for the measurement of Q_{1d} in the top layer 12 m thick. Figure 10 shows the wavelets and associated spectra for the critical refraction measurement, for Q_{crit} at the base of the firn column. An independent measurement of Q near the surface, Q_{1Pg} was made using the primary reflection, PP, and its source ghost, pPP. Figure 11 (panels a-d) shows
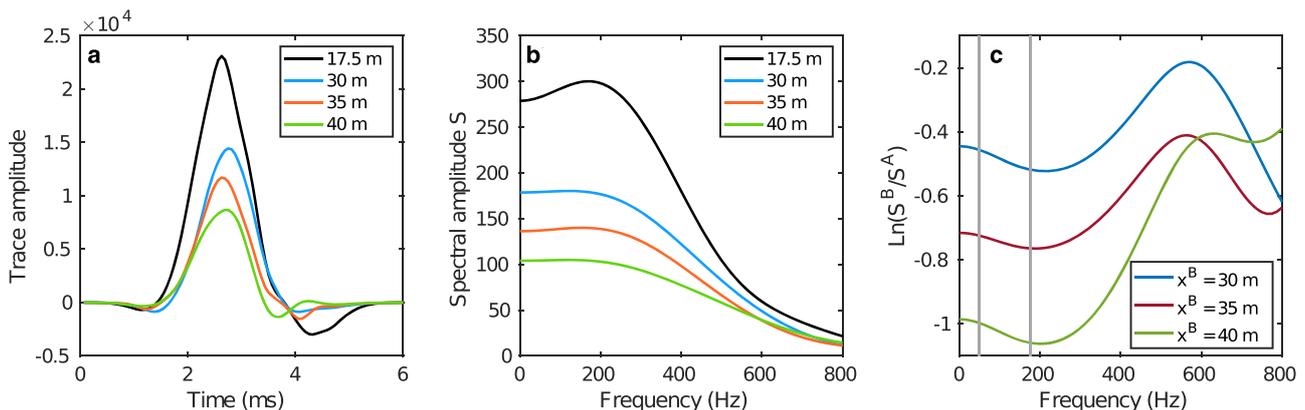
Figure 9. (a) Wavelets, (b) spectra and (c) logarithmic spectral ratios of diving waves used for the calculation of Q_{1d} in the uppermost layer (12 m thick). The spectral ratios are approximately linear within the chosen bandwidth of $50 - 175$ Hz, indicated in (c) by the grey vertical lines. The legends in a) and b) indicate source-receiver offsets of traces and their associated spectra. In (c), S^A is always the spectrum of the reference trace, at 17.5 m offset. x^B is the source-receiver offset of the comparison trace, with spectrum S^B, used to obtain the spectral ratio.
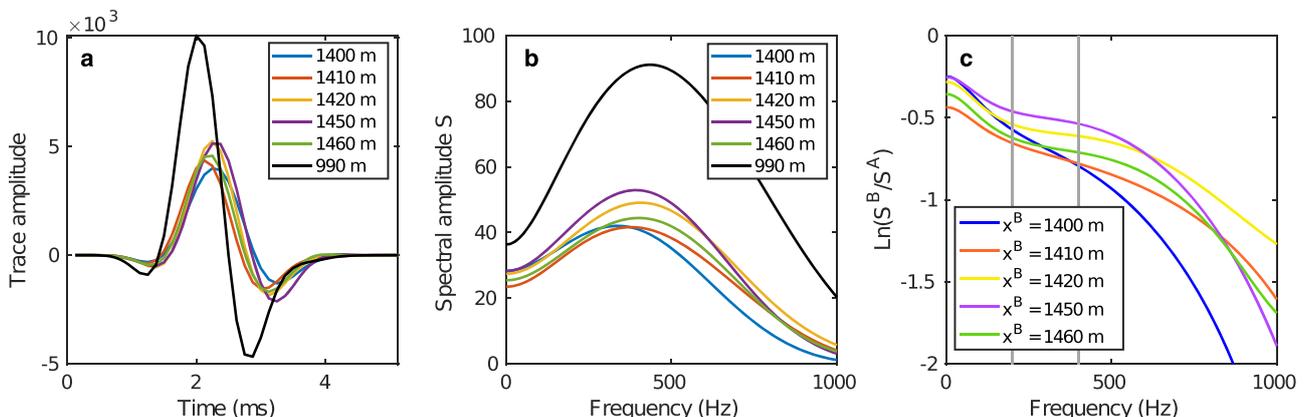
Figure 10. (a) Wavelets, (b) spectra and (c) logarithmic spectral ratios of critically refracted waves used for the calculation of Q at the base of the firn column, Q_{crit}. Legends (a) and (b) indicate source-receiver offsets of traces. The reference trace, which has spectrum S^A, is at 990 m offset. Legend (c) refers to the source-receiver offset of the comparison trace, x^B, used to obtain the spectral ratio. The grey bars in (c) show the bandwidth of spectral ratio measurement, $200 - 400$ Hz.
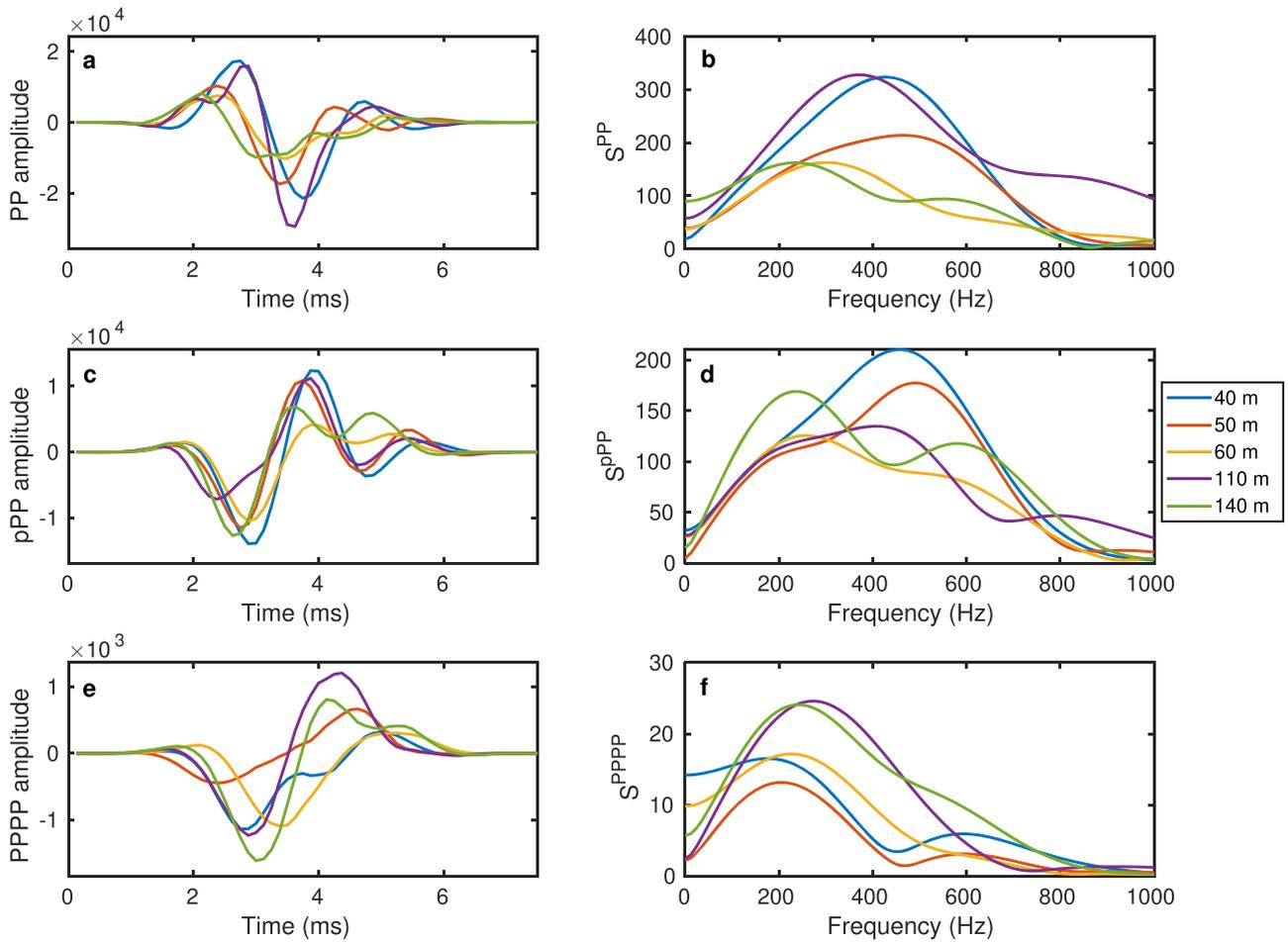
Figure 11. Wavelets and spectra recorded from buried-shot data. Primary reflection PP (a, b), its ghost pPP (c, d), and its first multiple PPPP (e, f).
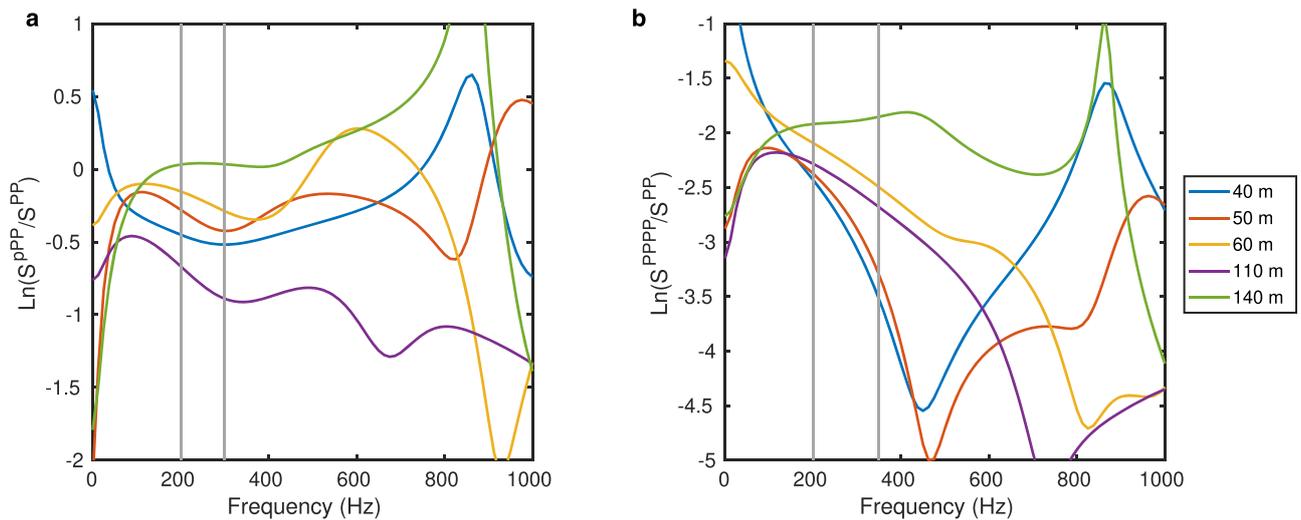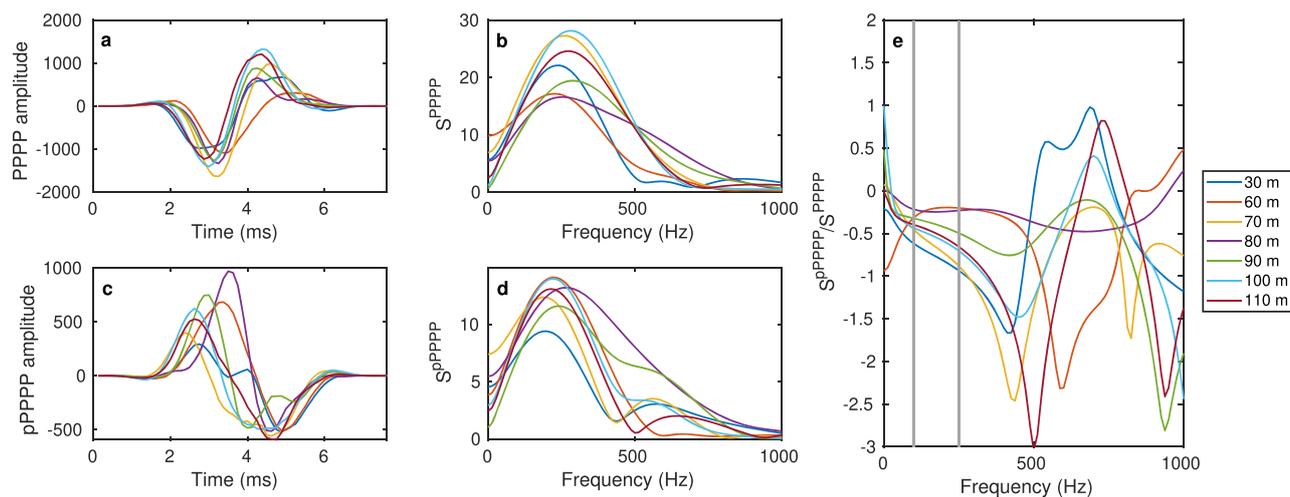

Figure 12. (a) Logarithmic spectral ratios of the primary and its ghost (pPP), used for the calculation of Q_{1pg}. (b) Logarithmic spectral ratios of the primary (PP) and first multiple reflections (PPPP), used for the calculation of Q_{tot}. Legend indicates source-receiver offset. The grey bars indicate the bandwidths used for Q measurement, (a) $200 - 300$ Hz, and (b) $200 - 350$ Hz.

these wavelets and their spectra, and Figure 12a shows the associated spectral ratios, along with the bandwidth of measurement. A measurement was also made over the entire ice column of Q_{tot}, using the primary and its first multiple (PPPP). These wavelets and spectra are shown in Figure 11 (panels e and f),

with associated spectral ratios in Figure 12b. Finally, a third measurement was made of Q close to the surface, Q_{1mg}, from the first multiple and its ghost, pPPPP. Figure 13 shows these wavelets, their spectra and associated spectral ratios. Table 5 shows the bandwidth used for each measurement.

Figure 13. (a) Wavelets and (b) spectra of the first multiple (PPPP) used for calculation of Q_{1mg}. (c) Wavelets and (d) spectra of the first multiple ghost (pPPPP) used for calculation of Q_{1mg}. (e) Logarithmic spectral ratios used to calculate Q_{1mg}. Legend indicates source-receiver offset of each ghost/multiple pair. Grey bars in (e) represent the bandwidth used for Q measurement, $100 - 250$ Hz.

Table 5. Bandwidths used for each spectral ratio measurement

Measurement	Frequency range (Hz)
Q_{1d} in uppermost layer (direct wave)	50–175
Q_{1pg} in uppermost layer from PP/pPP	200–300
Q_{1mg} in uppermost layer from PPPP/pPPPP	100–250
Q_{2-4} from layer stripping	200–450
Q_{crit} from critical refraction	200–400
Q_{tot} from primary and first multiples	200–350